

Transient hillslope erosion in slow evolution landscapes

Vincent Godard, Salgado A., L Siame, Jules Fleury, Team Aster

▶ **To cite this version:**

Vincent Godard, Salgado A., L Siame, Jules Fleury, Team Aster. Transient hillslope erosion in slow evolution landscapes. Earth Surface Processes and Landforms, 2021, 46 (12), pp.2485-2500. 10.1002/esp.5190 . hal-03346897v2

HAL Id: hal-03346897

https://amu.hal.science/hal-03346897v2

Submitted on 16 Nov 2021

HAL is a multi-disciplinary open access archive for the deposit and dissemination of scientific research documents, whether they are published or not. The documents may come from teaching and research institutions in France or abroad, or from public or private research centers.

L'archive ouverte pluridisciplinaire **HAL**, est destinée au dépôt et à la diffusion de documents scientifiques de niveau recherche, publiés ou non, émanant des établissements d'enseignement et de recherche français ou étrangers, des laboratoires publics ou privés.

Transient hillslope erosion in slow evolution landscapes

Godard V.[1,2,a], Salgado A.[3], Siame L.[1], Fleury J.[1] and ASTER Team[1,*]

November 16, 2021

[1]Aix-Marseille Univ, CNRS, IRD, INRAE, Coll France, CEREGE, 13545, Aix-en-Provence, France
[2]Institut Universitaire de France (IUF), 75231, Paris, France
[3]Department of Geography, Minas Gerais Federal University, CEP 31270-901 Belo Horizonte MG, Brazil

[a] Corresponding author : godard@cerege.fr
[*] Georges Aumaître, Didier L. Bourlès, Karim Keddadouche
Published in V., Godard, A., Salgado, L., Siame, J., Fleury & ASTER Team (**2021**) Transient hillslope erosion in slow evolution landscapes. *Earth Surface Processes and Landforms*, 46(12), 2485-2500 (10.1002/esp.5190)

Abstract

Transient evolution and adjustment to changing tectonic and climatic boundary conditions is an essential attribute of landscapes and characterizing transient behavior is a key to understand their dynamics and history. Developing new approaches to detect such transience has been explored by various methods, in particular to identify landscape response to Late Cenozoic and Quaternary climatic changes. Such studies have often focused on regions of high relief and/or active tectonic activity where interferences between tectonic and climatic signals might complicate the interpretation of the observations. We investigated the case of the hillslopes of the Serra do Cipó quartzitic range in SE Brazil in order to detect and quantify transience in a tectonically-quiescent landscape over 100 ka timescales. We determined hilltop curvature from a high resolution Digital Surface Model derived from Pléiades imagery and measured cosmogenic nuclide concentrations (^{10}Be and ^{26}Al) at these hilltop

sites. We compare both observations with predictions of hillslope diffusion theory, and observe a distinctive signature of an acceleration of denudation. We performed a joint inversion of topographic and isotopic data to retrieve an evolution of hillslope sediment transport coefficient through time. The timing of the increase in denudation cannot be unequivocally associated with a single climatic event but is consistent with climatically-modulated important fluctuations in precipitation and erosion in this area during Middle and Late Pleistocene.

1 Introduction

The Earth surface acts as a major interface between internal and external geodynamics, and is the focus of many investigations concerning the complex network of processes connecting surface processes, tectonics and climate [e.g. Champagnac et al., 2012]. Notably, a key element of this system is the degree of coupling between climatic variations and denudation, which is fundamental to assess the strength of many postulated feedbacks between the atmosphere and the dynamics of weathering, sediment production and transport across continental surfaces. Over short time scales, many observations support the key role of temperature and precipitation conditions in directly controlling the modes and rates of weathering of materials transiting through regolith profiles, as well as their export across and beyond hillslopes domain [e.g. Gaillardet et al., 1999; Hales and Roering, 2005; Gabet et al., 2008; West et al., 2014]. However, when integrating these processes over larger spatial and temporal frames, highly contrasting propositions have been made concerning the actual relationship between surface processes acting on continental relief and climatic evolution, over the Late Cenozoic. In particular, an important question still actively debated concerns whether or not Late Cenozoic cooling was associated with a global increase in denudation rates [e.g. Herman and Champagnac, 2016; Willenbring and Jerolmack, 2016; Norton and Schlunegger, 2017], suggesting that additional investigations

using novel methodologies are needed to better resolve denudation variations and transient landscape dynamics through time.

Regions of high relief or tectonic activity have often been the primary target of studies focusing on climate-denudation links, using the sedimentary archives resulting from the erosional fluxes in such areas [e.g. Charreau et al., 2011; Lenard et al., 2020]. However, important limitations can be encountered in this type of settings, such as high denudation rates reaching the analytical limits of many measurement methods, or gaps in the sedimentary records and stochastic events introducing a high degree of variability in the denudation signal. Additionally, temporal and spatial variations of the tectonic boundary condition can be difficult to deconvolve from the record and complicate interpretations in terms of climatic influence on surface processes.

Conversely, areas of low tectonic activity may provide propitious conditions allowing the investigation of the coupling between climate variations and surface processes. However, long-duration continental sedimentary archives, spanning several 100s ka or Ma, are often scarce in such settings so alternative approaches are required to develop longer-term records of landscape transience and assess its link with climatic evolution [Struck et al., 2018]. When measuring active denudation, as opposed to paleo-denudation records in sedimentary archives, slow landscape evolution also implies long integration timescales for most geochronological techniques, such as cosmogenic nuclides, which might provide insights on the dynamics of surface processes over 100s ka to several Ma. This time frame is at least one order of magnitude longer to that usually encountered in active orogenic settings.

Terrestrial Cosmogenic Nuclides (TCN) are one of the most widely used tools to constrain the distribution of denudation rates at the Earth surface over 1 ka-1 Ma timescales [von Blanckenburg, 2005]. Attempts to recover information on past denudation conditions have mostly focused on TCN time-series in the sedimentary record. However, combinations of several cosmogenic nuclides, with different decay constants, offer the possibility to identify

transient dynamics resulting from changes in denudation rates through time [Mudd, 2016]. For example, the promising ^{10}Be-^{14}C pair has been used to decipher complex dynamics of surface processes over Holocene time scales [Hippe, 2017; Skov et al., 2019]. The more common ^{26}Al-^{10}Be system, which is classically used for burial dating studies, is much less sensitive to fluctuations of denudation on this time frame [Mudd, 2016], but has been shown to offer important insights over longer time scales [Knudsen and Egholm, 2018; Struck et al., 2018], and its actual potential to decipher transient denudation evolution in slow denudation landscapes needs to be explored more systematically.

Independent of chronological approaches, another way to characterize transience in landscapes, resulting from changes in denudation or incision processes, is the study of the imprint of such perturbations on their morphology. Such approaches has been intensively used in fluvial systems , with the analysis of river long-profiles [e.g. Roberts and White, 2010; Fox et al., 2015], and the increasing availability of high resolution topographic data has paved the way for similar developments in the hillslope domain [Roering et al., 2007; Hurst et al., 2012, 2013; Grieve et al., 2016b; Mudd, 2016]. Notably, the combination of TCN data with high resolution hillslope morphological analysis has proven to be a fruitful source of information on landscape dynamics and their response to past perturbations [Godard et al., 2019].

In this study, we investigated the slowly eroding quartzitic landscapes of the Serra do Cipó Range in Minas Gerais, Brazil, by performing both high resolution morphometric analysis and cosmogenic nuclides concentration measurements (^{10}Be and ^{26}Al) at hilltop sites. The observed relationships between these parameters imply an important acceleration of denudation over 100s ka timescales and illustrate a new approach to probe into the transient dynamics of landscapes as well as expanding our knowledge of Quaternary paleoclimate of the central-eastern portion of South America.

2 Theoretical background

We present here the key concepts and ideas supporting our analysis of transient hillslope evolution in the Serra do Cipó. As reviewed by Mudd [2016], transient dynamics is a fundamental attribute of landscapes involving changes in their morphology, sediment fluxes or rates of denudation, and diagnostic observations can be made on these properties to identify such transient state in terms of deviation from morphological or erosional steady states. In the case of hillslopes, insights can be obtained from high resolution morphometric analysis of their shape or from denudation rates calculated from Terrestrial Cosmogenic Nuclides (TCN) concentration measurements in bedrock or stream sediments, which are two types of observations we combine in our study.

2.1 Hillslope erosion formulation

Roering et al. [1999] proposed an hillslope transport model, where sediment flux q_s is non-linearly dependant on topographic gradient dz/dx,

$$q_s = \frac{-K(dz/dx)}{1 - [(dz/dx)/S_c]^2}, \tag{1}$$

where K is a transport efficiency, or diffusion, coefficient, z is the elevation of the topographic surface, x the horizontal coordinate and S_c a threshold gradient. Numerous field investigations have supported the validity of this formulation in high relief landscapes [e.g. Ouimet et al., 2009; DiBiase et al., 2010]. In part of the landscape where topographic gradients are small compared to the threshold S_c this relationship can simplify as,

$$q_s = -K\frac{dz}{dx}, \tag{2}$$

Equations 1 and 2 are Geomorphic Transport Laws [Dietrich et al., 2003], which can be combined with a continuity statement,

$$\frac{dq_s}{dx} = \beta E, \tag{3}$$

with β the rock-to-regolith density ratio and E the long-term denudation rate, which is equal to rock uplift rate when steady state is achieved. Combining equations 2 and 3 yields,

$$E = \frac{KC_{HT}}{\beta}, \tag{4}$$

where C_{HT} is hilltop curvature, the second-derivative of the topographic surface. Equation 4 connects together two fundamental and distinct types of observations, which can be made about landscapes: measurements of their spatial topographic properties, in this case C_{HT}, and measurements of their temporal rate of evolution, in this case erosion rate E. For a given landscape, assessing whether these two types of observations can be reconciled within the framework of equation 4 can be used as a test of the underlying steady-state assumption. It should be noted that equation 4 was derived for the particular case of a ridge-like hillslope system. In the following, we will rather consider isolated hills and a radial symmetry for the hillslopes, which implies a slight modification of equation 4 [Anderson, 2002],

$$E = 2\frac{KC_{HT}}{\beta}. \tag{5}$$

2.2 Detection of transience from the confrontation of morphometric and TCN data

Terrestrial Cosmogenic Nuclides (TCN) are now routinely used for the determination of denudation rates in a variety of settings, as their steady-state concentration C in various

materials, such as stream sediment or outcropping bedrock, can be related to denudation rate E with,

$$C = \sum_i \frac{P_i}{\frac{E\rho}{\Lambda_i} + \lambda}, \tag{6}$$

with P_i the TCN production rate at the surface, ρ the material density, Λ_i the cosmic ray attenuation length and λ the decay constant for the considered nuclide. Subscripts i refers to the various production pathways, such as spallation by neutrons or muons capture. The integration time scale of these denudation rate measurements is usually calculated as the time required to erode a thickness equivalent to the neutrons attenuation length-scale, or ∼60 cm in most situations [von Blanckenburg, 2005]. It results in a wide range of integration windows from Ma to ka timescales for denudation rates ranging from 1 to 100 m/Ma, respectively. This dependency of integration time on denudation rates implies that sites with different denudation rates will respond more or less rapidly, in term of TCN-derived denudation rates, to perturbations of similar amplitude, and can be used to identify transient adjustment in landscapes as we illustrate below.

If a local cosmogenic nuclides steady state is achieved at the hilltop scale, the relationship between denudation rate E and hilltop curvature C_{HT} is linear and set by equation 5, assuming a spatially constant value for the sediment transport coefficient K (Fig. 1). Transience resulting from a change in the sediment transport coefficient through time can be detected by the non-alignment of the E vs C_{HT} or [^{10}Be] vs C_{HT} relationships to theoretical steady-state predictions. For the case of a slow denudation landscape, we assume that hillslope morphology does not change significantly over a 100 ka time-scale, and do not take into account eventual feedback between denudation and hilltop curvature.

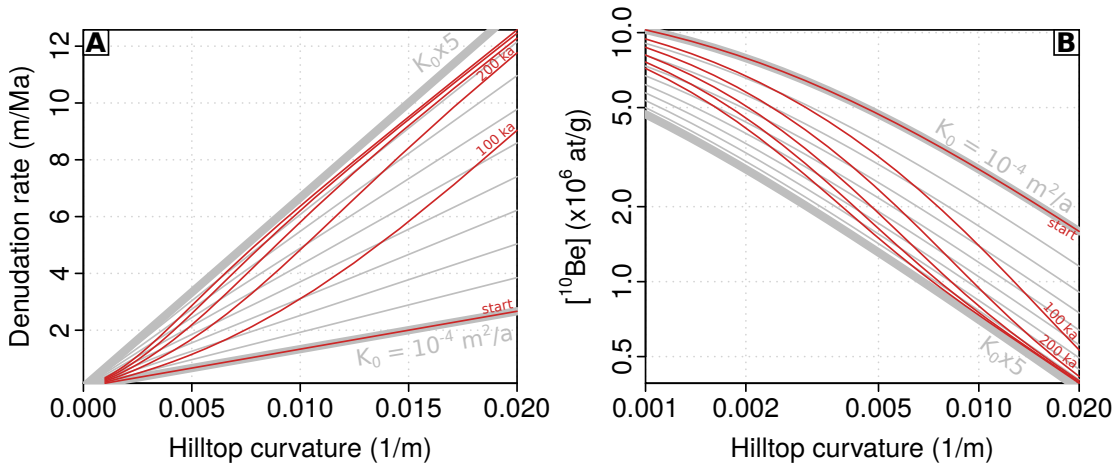


Figure 1: Illustration of the manifestation of transience in landscapes from the confrontation of cosmogenic nuclide data with high resolution topographic metrics. (A) Evolution of the relationship between hilltop curvature (C_{HT}) and ^{10}Be-derived denudation rate E, as a response to a 5-fold increase in sediment transport coefficient K. Thick grey lines are the starting and final steady-state situations. Thin grey lines are steady state relations for intermediate sediment transport coefficients (equation 5). Red curves display the transient evolution at 100 ka intervals. (B) Same as previous panel but for ^{10}Be concentration against C_{HT} (log axes). Note that we consider hillslope morphology, and thus hilltop curvature, to be stable over a time scale of a few 100s ka. This approximation is justified by the hillslope response time of the order of 1 Ma implied by the low sediment transport coefficient considered here.

2.3 Detection of transience from TCN pairs

As discussed by Mudd [2016], independently of morphological considerations, transience in denudation can also be detected by the use of pairs of cosmogenic nuclides with different decay constants. ^{10}Be-^{26}Al is the most widely used TCN pair, notably in burial dating applications [Granger and Muzikar, 2001]. However, their decay constant are of the same order of magnitude, which greatly limit the sensitivity of this system for the identification of transient adjustment conditions [Mudd, 2016]. Instead, this has oriented research efforts toward the ^{10}Be-^{14}C pair as the most promising system to resolve recent changes in denudation [Hippe, 2017; Skov et al., 2019; Hippe et al., 2021]. Nevertheless, it should be noted that in the particular case of slowly eroding landscapes, where the ^{10}Be and ^{26}Al half-lives are comparable with the TCN denudation integration timescale, the amplitude of the deviation of isotopic ratio away from steady-state denudation predictions can become analytically resolvable (Fig. 2). This deviation is particularly noticeable for an increase in denudation rate, as it significantly lowers the ratio below the steady-state denudation curve. The time-scale of the perturbation being also dependent on the denudation rate, the transient response can thus be observed over a few 100s ka in the case of slowly evolving landscapes (1 m/Ma).

3 Settings

Our study area is located in the Serra do Cipó national park, in the highlands of the Brazilian Southeast. The Serra do Cipó mountain is a narrow (30-km wide) quartzitic range located in the southern portion of the Espinhaço Range (Fig. 3), which is the most extensive and continuous Precambrian orogenic belt of the South American Platform and originated 600 Ma ago during the Brasilian Orogeny [Magalhães Junior et al., 2015]. The Espinhaço Range is an important hydrographic and landscape divider in South America.

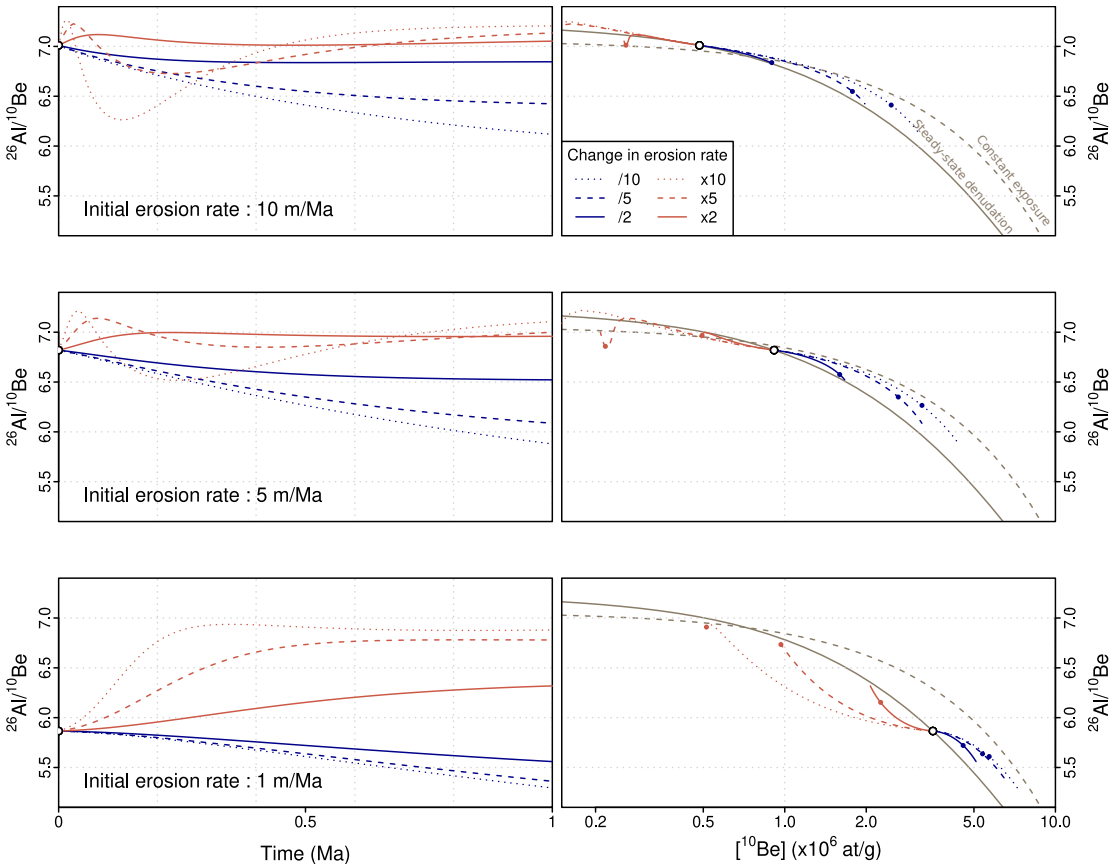


Figure 2: Responses of ^{10}Be and ^{26}Al surface concentrations and ratio to 2, 5 and 10-fold increases or decreases in denudation rates. Left panels display the evolution through time of the ^{26}Al/^{10}Be ratio, since the onset of the perturbation. Right panels display the corresponding evolution in a two-nuclides plot. White and colored circles indicate the starting points and 0.5 Ma mark, respectivelly. Solid and dashed brown curves correspond to expectations for steady-state erosion and a constantly exposed surfaces, respectively. Production rates are calculated for the average conditions at the sampled sites in the Serra do Cipó (Fig. 3), using a time-independent scaling scheme [Stone, 2000].

To the west is located the large hydrographic basin of the São Francisco River, which drains a craton characterized by smooth relief, semi-humid climate, and savanna vegetation. To the east, drainage is organized around smaller watersheds, such as the Doce and Jequitinhona hydrographic basins, that drain a half-orange hills plateau-type landscape, under humid climate and tropical forests [Salgado et al., 2019].

After its uplift during the Brasilian Orogeny, the Serra do Cipó has not been subjected to new orogenic phases and the subsequent erosion of the range resulted in a relief characterized by a wide quartzitic plateau (average elevation 1200 m), comprising a large sequence of ridges, reaching 2000 m in altitude, depressions and dissected fluvial valleys. There are no evidence of a direct impact of the opening of the South Atlantic on our study area. Although landscape properties are globally homogeneous across the Serra do Cipó, the portion of the range that drains towards the Doce River is more dissected than that draining into the São Francisco River.

Nowadays, the climate of Serra do Cipó Range is mesothermal, with Mean Annual Temperature between 18^{o}C-19^{o}C and Mean Annual Precipitation ranging from 1250 to 1550 mm, as well as dry winters and wet summers. However, there are lines of evidence, from pedological and geomorphological records, that the region underwent many climatic changes during the Holocene and late Pleistocene, with occurrences of periods wetter and dryer than the present-day conditions [Chueng et al., 2019; Barros and Magalhães Junior, 2020; Silva et al., 2020].

Due to the great resistance of the quartzite bedrock to erosion, denudation rates are <6 m/Ma [Barreto et al., 2013; Peifer et al., 2020], soils are thin and poor, hosting the typical vegetation of Campos Rupestres, a high altitude rocky field biome [Magalhães Junior et al., 2015]. This combination of slow denudation rates and significant relief is well suited for the coupling of high-resolution morphometry and cosmogenic nuclides analyses due to long-integration time scales for denudation, a limited contribution of stochastic events to

surface processes, a limited storage of erosion products and long relief response timescales.

4 Methods

4.1 General sampling strategy

Our strategy was to select prominent sites on top of soil-mantled vegetation-free hillslopes (Fig. 4), where the observed denudation rates E and morphological properties such as hilltop curvature C_{HT} could be linked into the simple physical framework of equation 5 [Anderson, 2002; Hurst et al., 2012]. The slope of this relationship between E and C_{HT} is set by the sediment transport coefficient K and the rock-to-regolith ratio β.

We primarily selected regolith-mantled hilltop sites, with regular morphologies and no bedrock outcrops (Fig. 4A-B). We sampled quartz fragments resulting from the dismantlement of quartz veins embedded in the fine-grained quartzite bedrock and sandy regolith (Fig. 4C). At some sites, the quartz veins were directly outcropping, but not significantly protruding over the surface, and the quartz fragments were detached directly from the veins (Fig. 4D). At other sites, the veins were not directly outcropping, but covered by 10 to 20 cm of regolith. We observed that the quartz veins remain coherent and resistant during their exhumation toward the surface, whereas the fine grained quartzite bedrock is converted into sandy regolith. Site O is an exception, where we directly sampled the outcropping quartzite bedrock.

4.2 Cosmogenic nuclides analysis

Samples for ^{10}Be and ^{26}Al concentrations measurements were collected at 11 hilltop sites, by amalgamating 30 to 40 individual quartz vein fragments at the surface (except for site

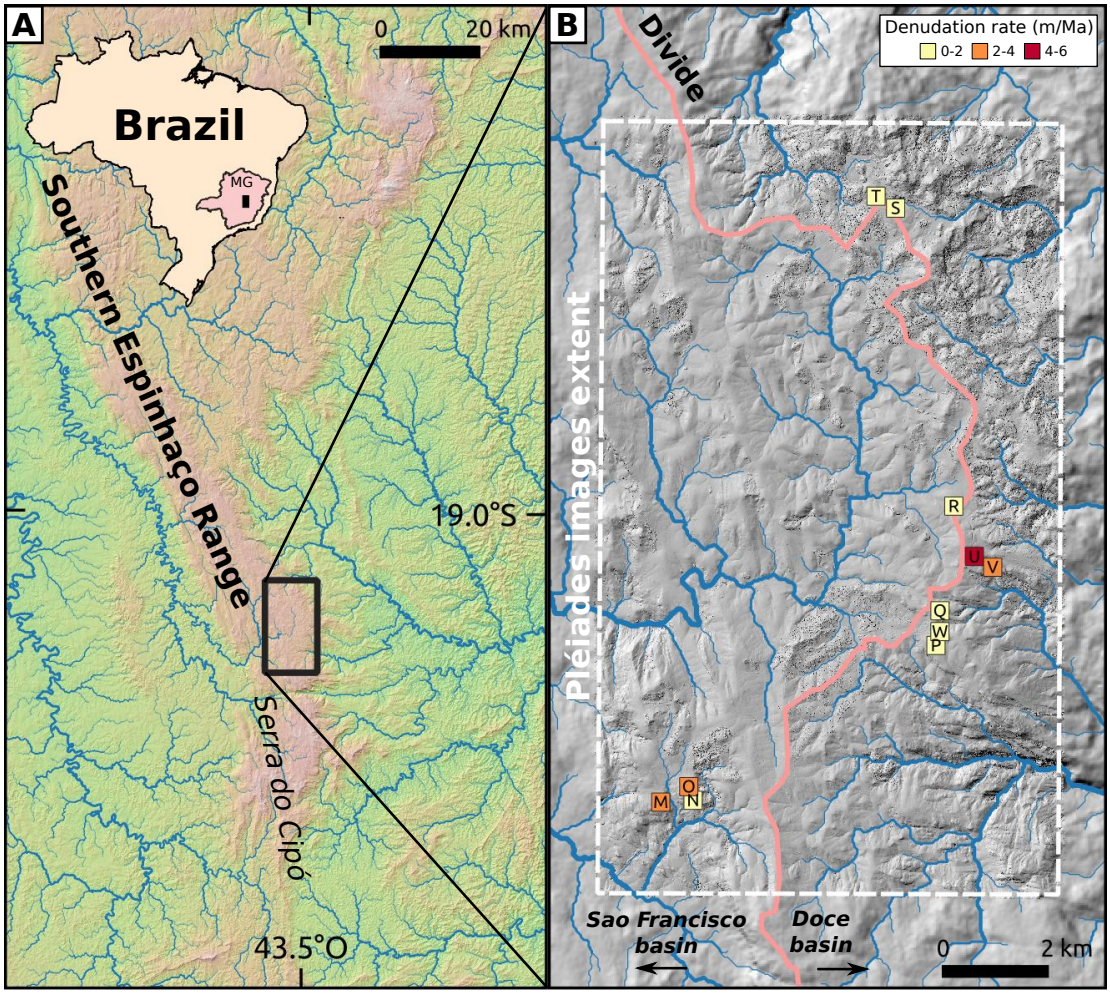


Figure 3: (A) Situation of the Southern Espinhaço Range in Minas Gerais State. (B) Location of sampled hilltop sites in the Serra do Cipó Range. Color scale indicates calculated steady-state denudation rates from ^{10}Be concentrations (m/Ma). Dashed rectangle is the extent of the Pléiades images triplet used to compute a high resolution Digital Surface Model (DSM). Pink line is the divide between the São Francisco and Doce river basins.

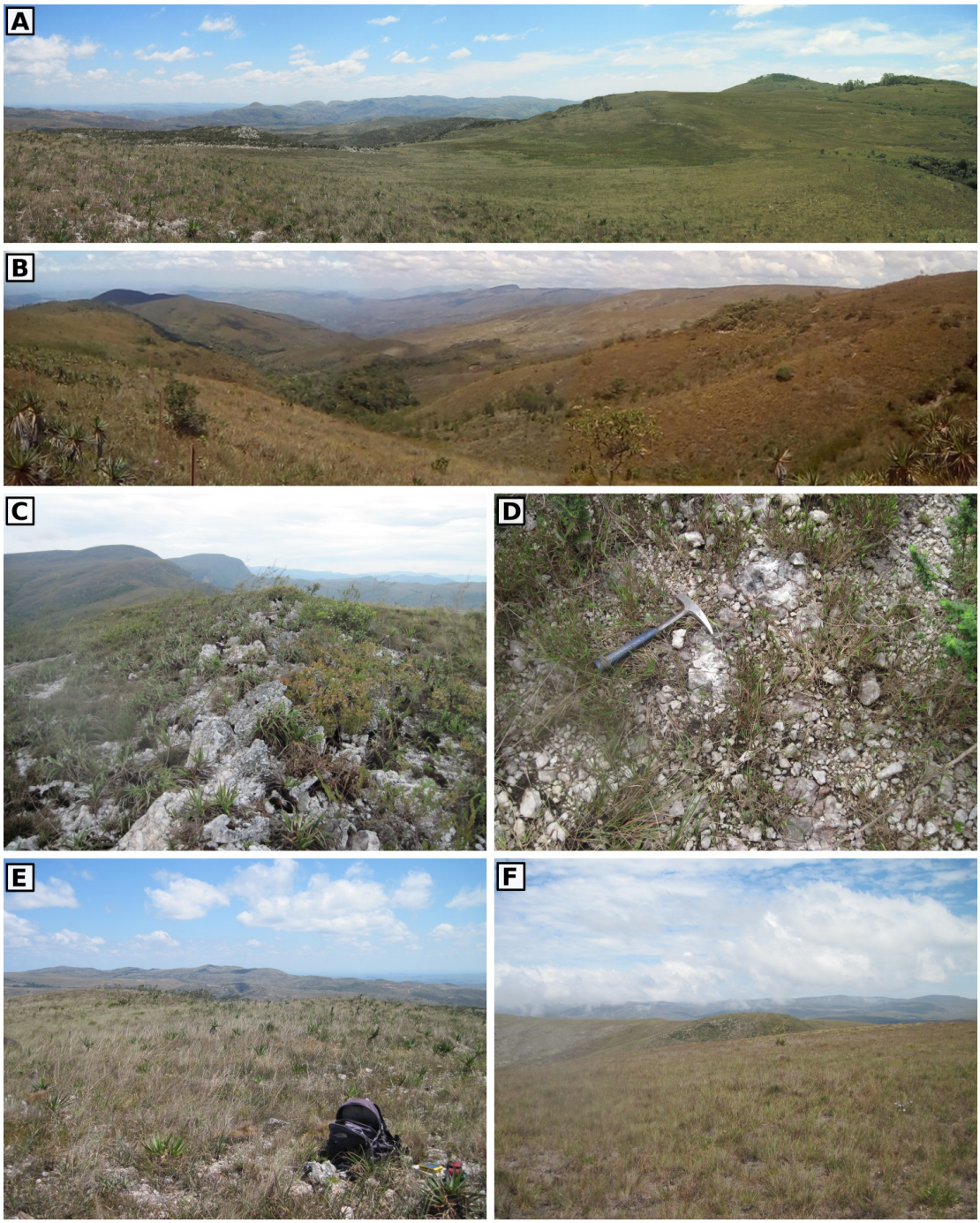


Figure 4: Sampling sites pictures. (A) View on Serra do Cipó landscape, toward the East from site M. (B) View on Serra do Cipó landscape, toward the East from site T. (C) Quartz vein at hilltop sampling site N. (D) Surface of hilltop sampling site W, with quartz vein embedded in the regolith and small quartz fragments. (E) Hilltop sampling site M. (F) View toward site W.

O). Samples were crushed and sieved to extract the 250-1000 μm fraction, which was submitted to sequential magnetic separations. The remaining fraction was leached with 37% HCl to remove eventual carbonate fragments. The samples were then repetitively leached with H_2SiF_6 and submitted to vigorous mechanical shaking until pure quartz was obtained. Decontamination from atmospheric ^{10}Be was achieved by a series of three successive leachings in concentrated HF, each removing 10% of the remaining sample mass [Brown et al., 1991]. After addition of Be and Al carriers, the samples were digested in concentrated HF. Be and Al were isolated for measurements using ion-exchange chromatography. ^{10}Be/^{9}Be and ^{26}Al/^{27}Al measurements were performed at the French AMS National Facility, located at CEREGE in Aix-en-Provence. All results and technical characteristics of the measurements and calculations are provided in tables 1 and 2.

For reference, and before investigating time-variations in denudation, we compute steady-state denudation rates (tables 1 and 2), which were calculated with the online calculator described in Balco et al. [2008] and the nuclide specific LSD scaling scheme of Lifton et al. [2014], using the CRONUS-Earth calibration dataset [Borchers et al., 2016] for the calculation of spallation production rates and muon production rates according to Balco [2017]. We used 160 g/cm^2 for the effective neutron attenuation length in rock, and a density of 2.65 g/cm^3. No shielding correction was considered for the hilltop sites we sampled.

4.3 Morphometric analysis

We acquired a triplet of Pléiades images covering our sampling area (Fig. 3B), and used photogrametric techniques to construct a 1 m resolution Digital Surface Model (DSM) and perform hilltop curvature calculations. Pléiades satellites provide panchromatic images with a 0.7 m resolution resampled at 0.5 m pixel size, and have the capacity to acquire multi-stereo views of a scene during the same orbit [Bernard et al., 2012]. In low vegetation settings, they provide an efficient and cost-effective alternative to airborne LiDAR to

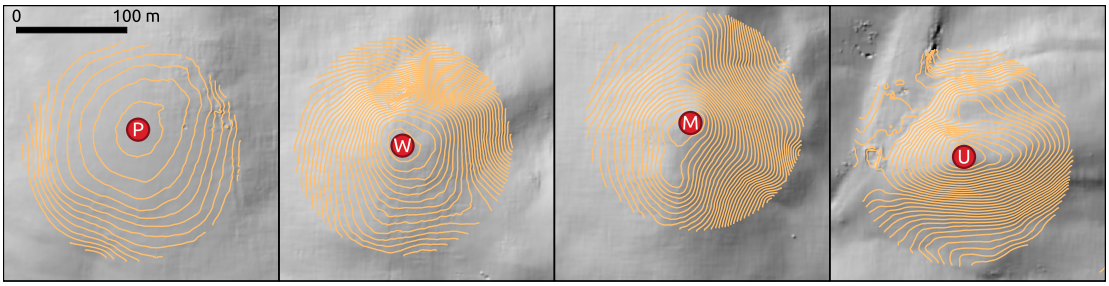


Figure 5: Shaded Pléiades Digital Surface Model (DSM) for 4 selected hilltop sites. Spacing of elevation contours is 1 m.

produce high-resolution Digital Elevation Models over large areas [e.g. Ansberque et al., 2016]. While this type of imagery, and derived topographic data, has been extensively used in tectonic geomorphology investigations since the launch of the satellites in 2011, its use in quantitative process-oriented geomorphological studies is less common [Godard et al., 2019]. A triplet of Pléiades images was acquired by instrument PHR1A on the 5th of July 2019 over a $\sim$250 km^2 area, covering the hilltop sites studied here.

The image triplet was processed with NASA AMES Stereo pipeline [Broxton and Edwards, 2008; Moratto et al., 2010] in order to produce a Digital Surface Model (DSM). We used the Rational Polynom Coefficients (RPC) provided with the images for the internal calibration of the pushbroom sensor. No Ground Control Points were used during the processing. The images were first roughly aligned by orthorectification on WGS84 datum using a SRTM Digital Elevation Model. Low-resolution disparity maps for couples of images were computed to determine coarse correspondence between pixels. Sub-pixel refinement was then performed using an adaptive window correlator [Nefian et al., 2009]. The disparity map was filtered by removing pixels with a value differing from the mean of their neighborhood by more than 3. The point cloud was triangulated and gridded to produce a 1-m resolution Digital Surface Model (Figs. 3 and 5).

In order to compute hilltop curvature C_{HT}, we fitted a quadratic surface to the DSM elevation over a circular window centered on the sampling point [Hurst et al., 2012]. The

equation of the surface is,

$$z = ax^2 + by^2 + cxy + dx + ey + f. \tag{7}$$

Topographic curvature C_{HT} is computed as the two-dimensional Laplacian of the quadratic surface as,

$$C_{HT} = 2a + 2b \tag{8}$$

The radius of the analysis window was chosen to be large enough to filter short-wavelength surface roughness, and small enough to avoid perturbation from the ridge-and-valley topographic signal [Lashermes et al., 2007; Roering et al., 2010; Hurst et al., 2012; Godard et al., 2016; Grieve et al., 2016a]. In our case, this radius was set at 10 m (Fig. 6). In order to account for uncertainties on the position of the sampling sites and the influence of small wavelength topographic fluctuations, we computed C_{HT} at each pixel within a 10 m radius of the sampling point, and then calculated the mean and standard deviation of these values.

4.4 Numerical modeling

We predicted the concentrations in ^{10}Be and ^{26}Al at the surface by considering the progressive accumulation of these cosmogenic nuclides during exhumation as a response to imposed time-varying denudation, using a Lagrangian point of view [Knudsen et al., 2019]. We used the CRONUS-Earth calibration dataset [Borchers et al., 2016] and nuclides specific time-dependent LSD scaling scheme [Lifton et al., 2014], for the calculation of spallation production rates. Muons production was computed following Model 1A and associated parameters from Balco [2017]. We used 160 g/cm^2 for the effective neutron attenuation length in rock, and a density of 2.65 g/cm^3.

The originality of our approach is that the denudation rate E at our sites of interest is

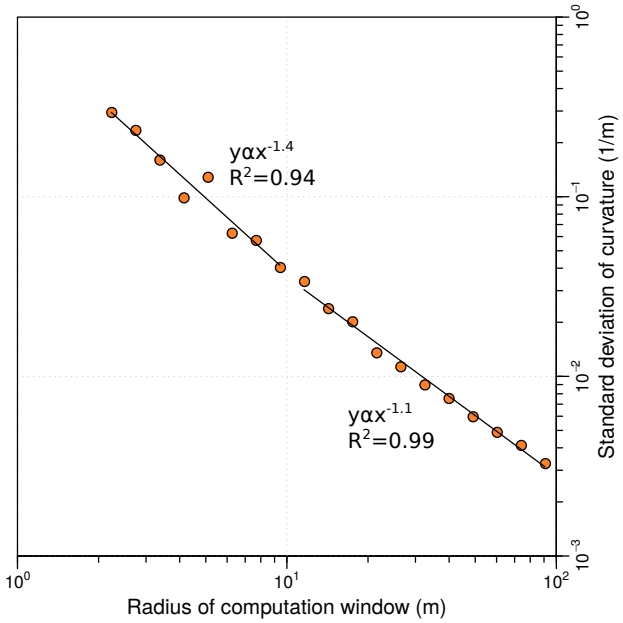


Figure 6: Evolution of the standard deviation of curvature as a function of the radius of the analysis window used to fit the quadratic surface of equation 7. 80×10^3 measurement points were sampled from the Pléiades DSM. A slight scaling break occurs at $\sim$10 m radius for the analysis window and this size is used in the curvature computation. We note that the scaling break in less pronounced than in the results of Roering et al. [2010], due to the gentler variations in elevation of the Serra do Cipó hillslopes and the absence of trees, as opposed to the rugged and densely forested landscape of the Oregon Coast Range.

computed from their measured hilltop curvature C_{HT} according to equation 5. This allows us to impose time-variations in denudation through changes in K, affecting all sites synchronously, rather than considering the evolution of denudation rates at each site individually. In other words, this allowed us to perform a joint inversion of a single K history to assess the changes in denudation through time, rather than dealing with the 11 independent denudation histories at each site separately.

We parameterized the evolution of the sediment transport coefficient K through time as a two-steps history, which is thus defined by three parameters : (1) the sediment transport coefficient K_1 during an initial slow denudation phase, (2) the sediment transport coefficient K_2 during a recent faster denudation phase and (3) the transition time T between the two phases. Similar scenarios of hillslope evolution based on a two-steps history for the sediment transport coefficient were explored by Roering et al. [2004] over shorter timescales, and allowed to capture the impact of a climate changing event while limiting the number of free parameters. A significant amount of scatter is expected in our dataset, which is usual in the type of complex natural system we are dealing with. Our forward model is based on a simplified definition of the problem, which does not account for numerous processes complicating hillslope dynamics and are not captured by idealized relationships such as equation 5. Additionally, the two-steps scenario we used is a coarse, but necessary, simplification of the actual denudation history. Such epistemic uncertainty is not represented by the measurement errors on either the ^{10}Be concentrations or hilltop curvatures. For that reason, we do not expect the modelled concentrations C_{mod} to be able to fit the observed concentrations C_{obs} within these measurement errors. We introduce a residual error σ_e as a 4$^{\text{th}}$ parameter which is sampled along the ones described above [Laloy et al., 2017], with a likelihood defined as,

$$L(K_1, K_2, T) = \frac{1}{\sqrt{2\pi}\sigma_e} \exp\left(\frac{-1}{2\sigma_e^2} \sum_{i=1}^{n} \left(C_{obs,i} - C_{mod,i}(K_1, K_2, T)\right)^2\right), \tag{9}$$

where n is the total number of observed TCN concentrations used in the inversion. We used a standard Monte Carlo-Markov Chain (MCMC) approach to move through the parameter space and estimate the posterior distributions [Metropolis et al., 1953].

5 Data

At hilltops, the measured ^{10}Be concentrations range from 0.8±0.02 to 6.9±0.1 10^6 at/g (Fig. 7A and table 1), which corresponds to steady denudation rates of 6±0.5 to 0.35±0.05 m/Ma, respectively. The ^{26}Al/^{10}Be ratios range from 4.4±0.1 to 6.4±0.2, with 6 samples plotting within the erosion island, slightly above the steady state erosion curve (Fig. 7A and table 2). These samples are evenly distributed over the range of observed ^{10}Be concentrations. One sample (R) presents an anomalously high ratio, which is impossible to obtain by TCN accumulation and decay. It is probably affected by an analytical issue on the determination of the ^{27}Al concentration, which is significantly higher than the rest of the dataset (except sample O). Only the ^{10}Be concentration will be used for this sample in the following. Finally, 4 samples display ratios clearly below steady-state denudation predictions, including the 3 samples with the lowest ^{10}Be concentrations.

At our sampling sites, measured hilltop curvatures span an order of magnitude from 0.005 to 0.039 m^{-1} (Fig. 7B and table 3). Denudation rates, calculated under a steady state assumption, increase with hilltop curvature. We note that sample O is slightly off the general trend and corresponds to the only site where we sampled the outcropping quartzite bedrock, instead of the quartz veins.

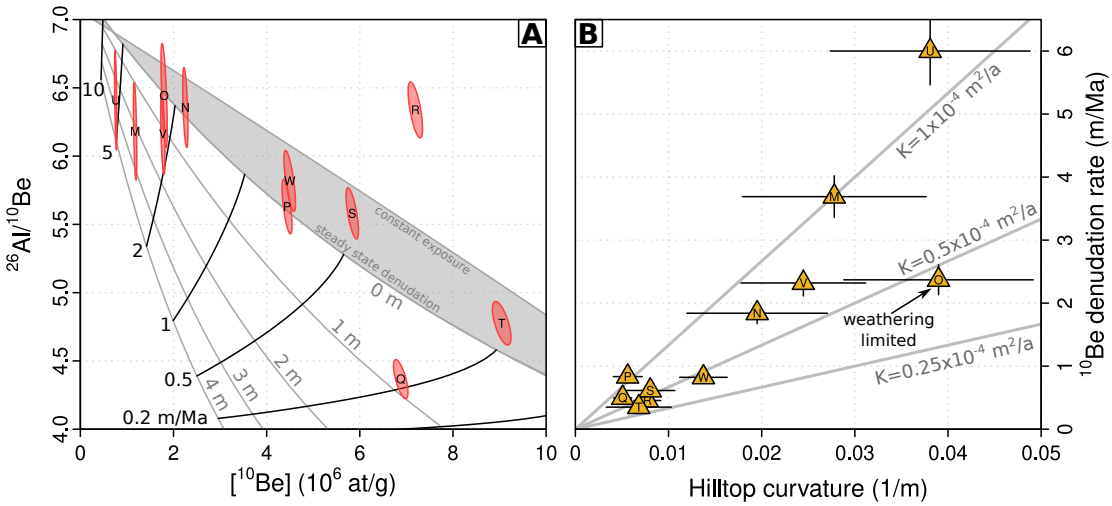


Figure 7: (A) Two-nuclides plot for the samples collected at hilltops (1σ confidence ellipses). See figure 3 for sites locations. Grey-filled area indicates the region between the steady-state surface denudation and constant exposure scenarios. Grey and black lines correspond to various regolith mixing-depth and denudation rates, respectively, according to the model of Foster et al. [2015]. Scaling according to Stone [2000]. (B) Denudation rate calculated from measured ^{10}Be concentrations as a function of hilltop curvature computed from the Pléiades DSM. Grey lines correspond to equation 5 with various values of the sediment transport coefficient.

6 Discussion

6.1 Interpretation of observed TCN concentrations

The denudation rates calculated under a steady-state assumption span a large range, from 0.5 to 6 m/Ma. Barreto et al. [2013] reported denudation rates of 1.8 to 2.4 m/Ma and 4.0 to 6.3 m/Ma for catchments located in the São Francisco and Doce river basins, respectively. The global range of denudation rates reported for these catchment wide denudation rates is largely overlapping with our local measurements near the drainage divide. We do not observe systematic gradient in denudation rates at our sites between the two sides of the divide, as in the results of [Barreto et al., 2013], and the diversity of denudation rates in our dataset probably reflects an underlying long-standing diversity in hillslope and hilltop morphologies across the relict landscape of the Serra do Cipó uplands.

Some of our samples present $^{26}Al/^{10}Be$ ratios that are significantly lower than steady-state denudation predictions (sites Q, M, U and V). Such low ratios are usually interpreted as reflecting temporary burial of the material [Granger and Muzikar, 2001] where, in the absence of TCN production, the differential rate of decay between the two isotopes is progressively lowering the ratio. However, such explanation is highly unlikely for our samples collected at the top of continuously eroding prominent hilltop sites, where there is no evidence for any significant potential for long-term storage and burial. Regolith mixing in slowly eroding soil profiles can also induce a lowering of $^{26}Al/^{10}Be$ ratios below the steady-state denudation line [e.g. Makhubela et al., 2019]. While this process could explain the measured ratio at site Q, it is difficult to reconcile with field observations at the other sites where we directly sampled outcropping veins. Furthermore, these three sites (M, U and V) display the highest denudation rates, and are eroding almost an order of magnitude faster than the slowest sites of the dataset. The last possible process to explain the observed low $^{26}Al/^{10}Be$ ratios at sites M, U and V is an increase of denudation rate [Struck et al.,

2018], which would dominantly impact the fastest sites with short integration time scales (100-200 ka, table 1) and much less the slowest sites, which average denudation over a longer time-frame (Fig. 2). Independent of any consideration on the morphology of the studied sites, our TCN data present evidence of transience and acceleration of denudation rates in the past. The amplitude and timing of such increase is however difficult to constrain from ^{26}Al-^{10}Be data alone.

6.2 Relationship between TCN data and hilltop morphology

The relationship between denudation rate E and hilltop curvature C_{HT} (equation 5) is not linear (Fig. 7B), as would be expected from hillslope diffusion theory [Anderson, 2002; Hurst et al., 2012]. No single sediment transport coefficient can explain the data within uncertainty, and we observe a systematic tendency for the sites with higher denudation rates (lower integration time scale) to plot on a higher K line, when compared to the slower ones. In line with our previous observations on the ^{26}Al/^{10}Be ratios, this constitutes an additional evidence for an acceleration of denudation over our area of interest (Fig. 1). We note that a recent large-scale compilation by Gabet et al. [2021] have also identified non-linearity in the relationship between C_{HT} and TCN-derived denudation rates but further investigations are needed to assess its signification in terms of hillslope dynamics.

In order to obtain more quantitative insights on this postulated acceleration of denudation, we tested a 2-stage denudation history defined by 3 parameters : the transition time between the slow and fast periods of denudation and their respective sediment transport coefficients (Fig. 8). We predicted ^{10}Be concentrations at the sites of interest for any combinations of these parameters, using the measured hilltop curvature (C_{HT}) to compute denudation rates evolution through time using equation 5, and perform a MCMC driven inversion. The sampling of the parameter space is driven by the Metropolis-Hasting algorithm, with an acceptance rate of 32%. We ran 16 independent chains, each 5×10^5, in

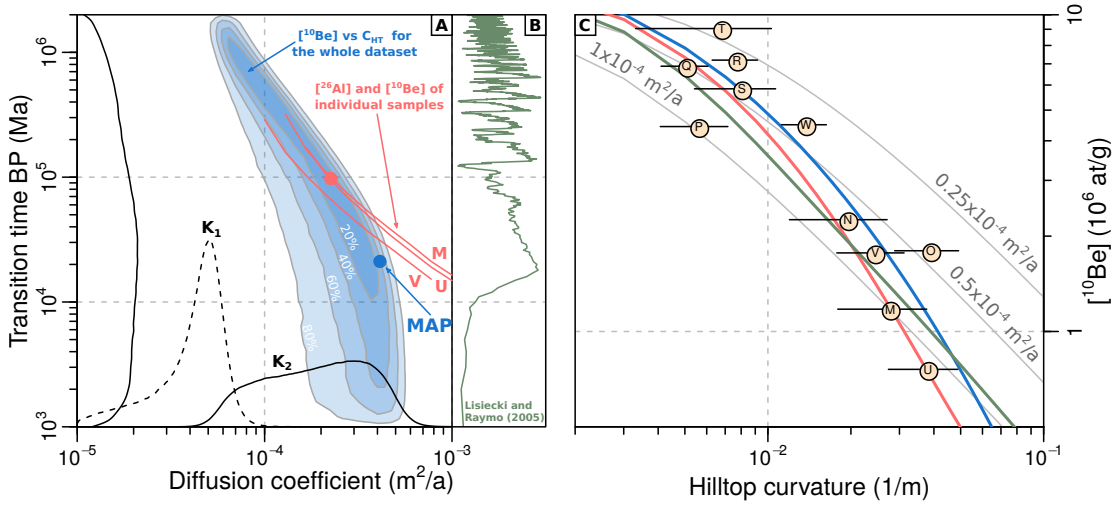


Figure 8: (A) Result of the MCMC inversion based on a 2-stages history set by 3 parameters: the initial (K_1) and final (K_2) sediment transport coefficients and the transition time T between the two. Blue shaded contours are highest posterior density region for T against K_2, and the filled blue circle indicates the Maximum Aposteriori Probability (MAP). Solid lines are marginal probability densities for K_2 and T, dashed line corresponds to K_1. Red lines correspond to parameters combination allowing to predict the ^{10}Be and ^{26}Al concentrations within 1σ of the measured values (K_1 is set at 4×10^{-5} m^2/a). Red filled circle is a manually set parameters combination. (B) Marine δ^{18}O stack from Lisiecki and Raymo [2005] (log time scale). (C) Comparison of hilltop curvature (C_{HT}) and ^{10}Be concentrations. Grey lines are predictions for different time-constant sediment transport coefficients scenarios. Blue and red curves correspond to the predictions associated with sets of parameters from the filled circles on panel A. Dark green curve corresponds to the predictions with a sediment transport coefficient evolution mapped on the δ^{18}O curve, ranging from 10^{-5} to 3×10^{-4} m^2/a.

length with a 10^4 length burn-in phase. The multivariate Potential Scale Reduction Factor is 1.001 suggesting convergence was achieved [Gelman and Rubin, 1992].

The inversion results support a low initial K value ($< 8 \times 10^{-5}$ m^2/a), followed by a very marked increase (5×10^{-5} to 5×10^{-4} m^2/a). A pronounced trade-off exists between the onset time of the second phase and the value of its sediment transport coefficient, which makes it difficult to directly confront these results with climatological and morphological records. Indeed, both an intense and recent phase with a transition as young as 10 ka or a much older up to 1 Ma event with lower sediment transport coefficient could provide

reasonable fits to the data (Fig. 8B). We note that solving for TCN accumulation using an simplified Eulerian approach [Knudsen et al., 2019] with exponential attenuation profile for muonic production and a time-independent scaling [Stone, 2000], instead of the Lagrangian scheme we used in our reference model, does not substantially modify the outcome of the inversion (Fig. 9B).

Additional independent constraints can be obtained from the low $^{26}Al/^{10}Be$ ratios of the fastest denudation sites Assuming an initial $K_1 = 4 \times 10^{-5}$ m^2/a, for each value of K_2 we computed the best transition time T allowing to explain both ^{10}Be and ^{26}Al concentrations within 1σ uncertainty, for each sample independently (Fig. 8A, red lines). For each of these samples (M, U, V), we observed the same tradeoff between K_2 and T as for the C_{HT}-^{10}Be inversion of the whole dataset. The lines defining the best K_2-T combinations for these ^{26}Al-^{10}Be data appears to intersect the region of maximum posterior density for the C_{HT}-^{10}Be inversion at a transition time $T \sim 100$ ka. Finally, a joint inversion of C_{HT}, ^{10}Be and ^{26}Al data for the whole dataset narrows down the range of probable transition time and is also consistent with a value close to 100 ka (Fig. 9C). As discussed below, this time scale for a postulated shift in surface dynamics is in agreement with reported environmental changes in the area, notably precipitation [e.g. Cruz et al., 2009b].

We note that our results could be affected by the processes occurring during the exhumation of the quartz fragments sampled at the surface. Notably, a mixing of these fragments in the regolith layer, rather than the monotonous exhumation toward the surface assumed in our models, would significantly impact their accumulation of cosmogenic nuclides through time [Granger et al., 1996; Makhubela et al., 2019]. As discussed above, we have numerous lines of evidence that those fragments result from the dismantlement of massive quartz veins, which remained mostly cohesive during their exhumation history embedded in the regolith, implying little mixing. The $^{26}Al/^{10}Be$ ratios of most of the high-concentration samples are not compatible with a significant mixing of the fragments in the regolith (Fig 7A), with the

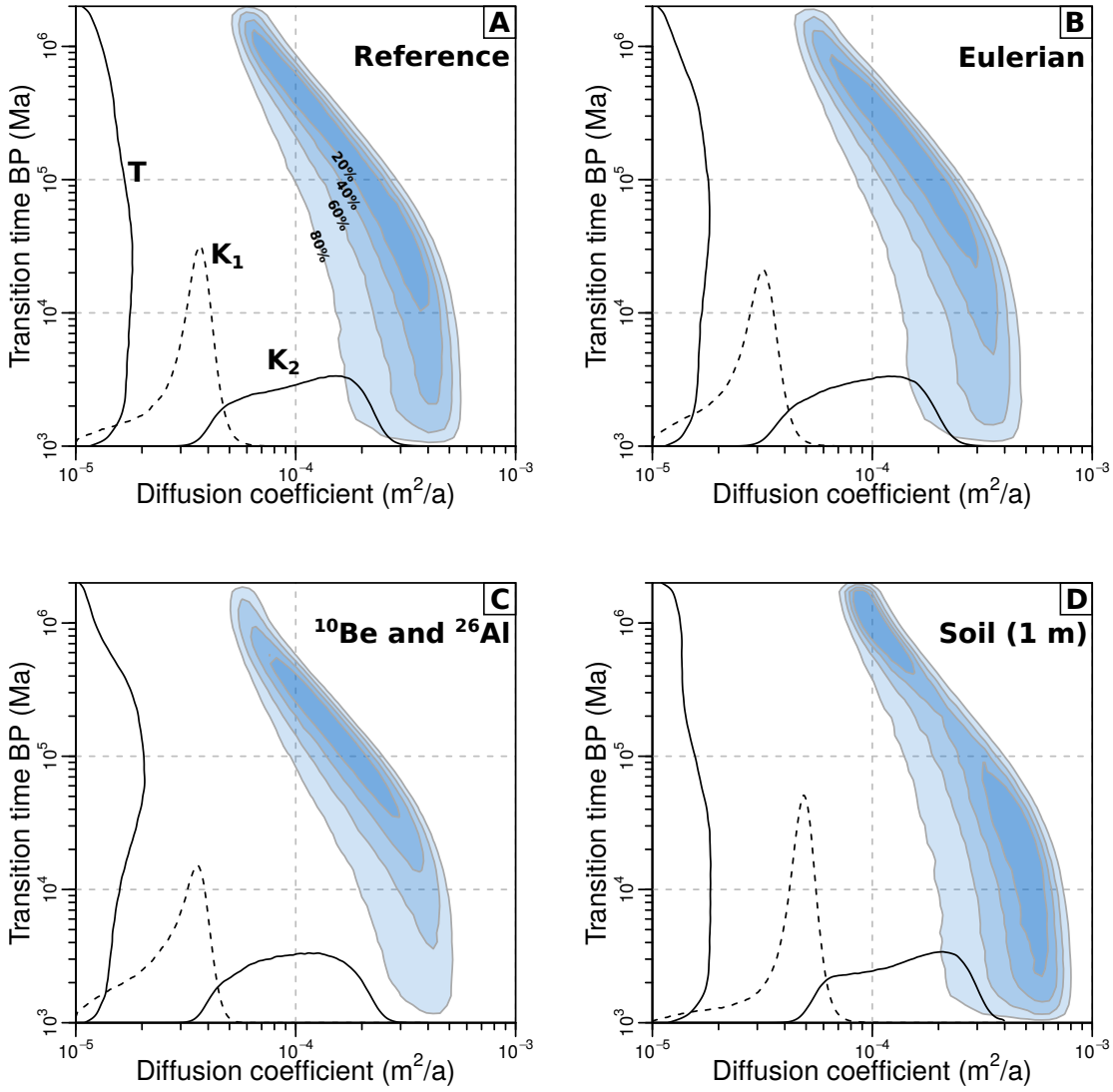


Figure 9: Tests of the influence of various aspects of the modelling approach on the inverted distributions for K_1, K_2 and T. (A) Reference model (same as Fig. 8). Result of a MCMC inversion based on a 2-stages history set by 3 parameters: the initial (K_1) and final (K_2) sediment transport coefficients and the transition time T between the two. Blue shaded contours are highest posterior density region for T against K_2. Solid lines are marginal probability density for K_2 and T, dashed line corresponds to K_1. (B) Same as reference model but forward problem is solved with an Eulerian approach [Knudsen et al., 2019], using the time-independent Stone [2000] scaling and an exponential model for the muonic production at depth, with parameters from Braucher et al. [2011]. This simplified and computationally much faster Eulerian scheme provides essentially the same results as the reference model. (C) Same as reference model but using both ^{10}Be and ^{26}Al concentrations (only ^{10}Be data is used in the reference model). (D) Same as reference model, but the density decreases to 1.7 during the last 1 m of the exhumation history, to test the influence of density change associated with a regolith layer.

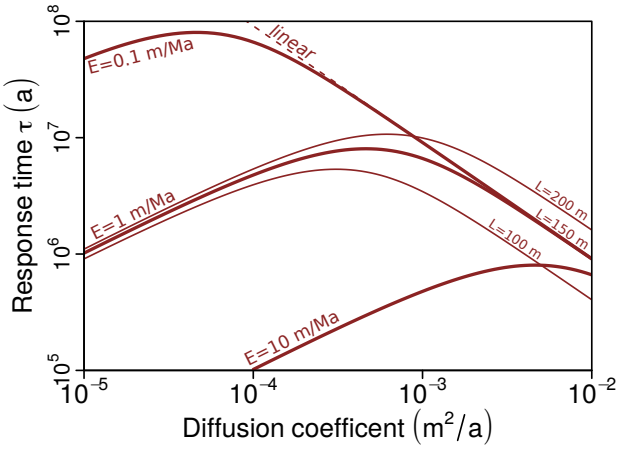


Figure 10: Adjustment time-scales of hillslopes based on linear (dashed lines) and non-linear (solid lines) evolution models [Roering et al., 2001; Hurst et al., 2012], for different values of the erosion rate E and hillslope length L.

exception of sample Q. We also note that our reference model is designed with a constant density during the exhumation history. In order to test the influence of a change in density when moving through the regolith for the final stage of exhumation [Struck et al., 2018], we tested the effect of a 1-m thick layer of density 1.7, and we observed that such modification does not substantially alter the general pattern retrieved from the inversion for the various parameters (Fig. 9D). It is important to note that our approach relies on the hypothesis that hillslope morphology does not change substantially over the investigated time period, so that there is no feedback between denudation and hilltop curvature, which is considered constant here. Calculated hillslope response times for the range of very low denudation rates and sediment transport coefficient considered here are at least several Ma, supporting the hypothesis of a stable landscape over the time-frame of the climatic perturbations scenarios we investigate (Fig. 10).

6.3 Comparison with regional climatic and geomorphic records

The two types of observations we made (C_{HT}-^{10}Be relationship and ^{26}Al/^{10}Be ratios) suggest a significant increase of denudation occurring over the last few 100s ka. However, it

is difficult to pinpoint an actual event from each approach alone. Indeed, onset of rapid denudation as young as a few 10s ka, close to the Last Glacial Maximum, or as old as 800 ka, near the Mid-Pleistocene Transition, provide comparable fits to the C_{HT}-^{10}Be data (Fig. 8). We note that we also used a very simplified 3-parameters definition of the evolution of K, which implies a single step-change and does not allow the possibility of multiple events or of a gradual change. We tested this type of scenario by mapping the evolution of the sediment transport coefficient on the δ^{18}O stack of Lisiecki and Raymo [2005], with a prescribed range of variations. Such evolution of K yields a relationship between C_{HT} and ^{10}Be concentrations that does not fit the data as well as the abrupt evolution associated with the 3-parameters scenarios. However, it still reproduces the general trend and in particular the fact that it does not correspond to a steady state situation (Fig. 8C, green line). When considered alone, the ^{26}Al/^{10}Be ratios of the high-denudation samples also display a similar tradeoff between T and K_2, but the combination with C_{HT}-^{10}Be inversion results significantly narrows down the range of likely age for the onset of the increase in denudation rates to 100-300 ka (Figs. 8 and S4).

There are lines of evidence supporting important Quaternary fluctuations of precipitation, temperature and vegetation in SE Brazil [Salgado-Labouriau et al., 1998; Behling, 2002; Ledru et al., 2005], and in particular in the Espinhaço Range [Chueng et al., 2019; Silva et al., 2020]. For example, precipitation has been shown to be strongly modulated by orbital fluctuations [Wang et al., 2007; Cruz et al., 2009a], with some speleothem records suggesting a wetter climate starting at 70 ka [Cruz et al., 2009b], a timing comparable with the transition time inferred from our inversion results. Early and Middle Quaternary geomorphological markers, such as river terraces, are often poorly preserved in the area, but display a strong climatic control on cycles of erosion and deposition [Barros and Magalhães Junior, 2020]. The hypothesis that climatic fluctuations is the main driver of the increase in denudation rates is reinforced by the fact that there was a reduction in in-

traplate tectonic activity beginning in the Middle Quaternary or earlier in the southeastern highlands of Brazil [Salgado et al., 2016]. This idea of a dominant climatic control is further reinforced by the non-linear E-C_{HT} relationship observed in figure 7, which can be considered as symptomatic of a top-down climatic forcing, where climatically-triggered changes in precipitation or vegetation modulate hillslope sediment transport coefficient. Conversely, a bottom-up perturbation associated with tectonically-driven base level changes would preserve the co-linearity of the samples in an E-C_{HT} plot. While we cannot unambiguously associate a particular event to our observations of transience in the landscape of the Serra do Cipó, they probably result from the integration of climatic fluctuations and an increased denudation trend over the Late Pleistocene.

6.4 Implications for the detection of transient evolution in landscapes

Combining the analysis of detailed high resolution hillslope morphometry with TCN data is a promising way to investigate landscape dynamics but has been only used in a limited number of situations [DiBiase et al., 2012; Hurst et al., 2012; Godard et al., 2019, 2020]. Such an approach allows to combine the two types of observation into a physical, process-based framework, such as equation 5, in order to test the underlying assumption and evaluate its limitations. Our study illustrates the potential of such an approach to identify transient dynamics in slowly eroding landscapes, and assess its links with climatically-driven top-down forcings. We take advantage of the differences in integration timescales of the two methods: a few 100 ka for TCN concentrations and of the order of 1 Ma for hilltop curvature measurements (Fig. 10), which allows to unravel time variations in the intensity of surface processes. Hilltops of the Serra do Cipó range display several evidences of Late Quaternary acceleration of erosion, as the relationship between ^{10}Be concentrations and

hilltop morphology, as well as the $^{26}Al/^{10}Be$ ratios, both displaying significant deviation from steady state predictions. There are however limits to the resolving power of such combination with respect to the details of denudation history that can be retrieved, which are manifest in the observed trade-offs between parameters (Fig 8A and 9). Using additional TCN, such ^{36}Cl or *in situ* ^{14}C might allow to extract more details about the denudation history. However, *in situ* ^{14}C has not yet been used to investigate such low denudation settings and modeling studies anticipate important limitations to its resolving power in such settings [Skov et al., 2019]. ^{36}Cl would require target minerals such has carbonates or feldspars which are not present in the setting we investigated, but might be feasible in granitic landscapes. While it does not provide a time-series for the evolution of denudation, our study illustrates the possibilities and potential of investigating paleo-denudation of slowly evolving landscapes in addition to the often explored tectonicaly active mountain ranges.

7 Conclusion

We studied the denudation of hilltop sites in the Serra do Cipó range, by collecting high resolution morphometric data and measuring ^{10}Be and ^{26}Al concentrations in surface materials. We compared our observations with prediction of simple hillslope diffusion theory for the relationship between morphological attributes and denudation rates derived from these TCN concentrations. We identified substantial deviation from steady state configuration, suggesting an important change in surface denudation over recent time periods, which results in the observed transient state. The originality of our approach is to conduct a joint inversion of both isotopic and morphometric data to derive the temporal evolution of the hillslope sediment transport coefficient. Our inversions suggest an important increase in the sediment transport coefficient and denudation rate over 100 ka timescale, which most

likely results from a modulation of soil transport efficiency of climatic origin. However, a trade-off between the timing of the acceleration and denudation intensity limits our ability to precisely pin point a specific climatic event. Our study illustrates the strong potential of landscape analysis that link geochronological and topographic data into a single physically-based framework, as for example hillslope diffusion theory. In our case, it allows to identify transient dynamics at the scale of hillslope, and the persistence of instabilities, which is key for longer-wavelength landscape-scale analysis of the influence of climatic and tectonic forcings.

Acknowledgments

This work was supported by CAPES-COFECUB (Research Project 869/15) and an IUF fellowship to VG. The ^{10}Be and ^{26}Al measurements were performed at the ASTER AMS national facility (CEREGE, Aix en Provence) which is supported by the INSU/CNRS, the ANR through the "Projets thématiques d'excellence" program for the "Equipements d'excellence" ASTER-CEREGE action and IRD. The Pléiades images used in this study were obtained through the DINAMIS framework and GEOSUD EQUIPEX. We thank Rodolphe Cattin for insightful discussions. Constructive comments by Simon Mudd, an anonymous reviewer and the associate editor greatly helped to improve this manuscript. This article is dedicated to the memory of our friend and colleague Didier L. Bourlès who sadly passed away during its preparation.

References

Anderson, R. S. (2002). Modeling the tor-dotted crests, bedrock edges, and parabolic profiles of high alpine surfaces of the Wind River Range, Wyoming. *Geomorphology*, 46(1-2):35–58.

Ansberque, C., Bellier, O., Godard, V., Lasserre, C., Wang, M., Braucher, R., Talon, B.,

de Sigoyer, J., Xu, X., and Bourlès, D. L. (2016). The Longriqu fault zone, eastern Tibetan Plateau: Segmentation and Holocene behavior. *Tectonics*, 35(3):565–585.

Arnold, M., Merchel, S., Bourlès, D. L., Braucher, R., Benedetti, L., Finkel, R. C., Aumaître, G., Gottdang, A., and Klein, M. (2010). The French accelerator mass spectrometry facility ASTER: Improved performance and developments. *Nuclear Instruments and Methods in Physics Research, Section B: Beam Interactions with Materials and Atoms*, 268(11-12):1954–1959. ISBN: 0168-583X.

Balco, G. (2017). Production rate calculations for cosmic-ray-muon-produced 10Be and 26Al benchmarked against geological calibration data. *Quaternary Geochronology*, 39:150–173. Publisher: Elsevier B.V.

Balco, G., Stone, J. O., Lifton, N. a., and Dunai, T. J. (2008). A complete and easily accessible means of calculating surface exposure ages or erosion rates from 10Be and 26Al measurements. *Quaternary Geochronology*, 3(3):174–195. ISBN: 1871-1014.

Barreto, H. N., Varajão, C. A., Braucher, R., Bourlès, D. L., Salgado, A. A., and Varajão, A. F. (2013). Denudation rates of the Southern Espinhaço Range, Minas Gerais, Brazil, determined by in situ-produced cosmogenic beryllium-10. *Geomorphology*, 191:1–13.

Barros, L. F. d. P. and Magalhães Junior, A. P. (2020). Late quaternary landscape evolution in the Atlantic Plateau (Brazilian highlands): Tectonic and climatic implications of fluvial archives. *Earth-Science Reviews*, 207(May):103228. Publisher: Elsevier.

Behling, H. (2002). South and southeast Brazilian grasslands during Late Quaternary times: A synthesis. *Palaeogeography, Palaeoclimatology, Palaeoecology*, 177(1-2):19–27.

Bernard, M., Decluseau, D., Gabet, L., and Nonin, P. (2012). 3D capabilities of PLEIADES satellite. *ISPRS - International Archives of the Photogrammetry, Remote Sensing and Spatial Information Sciences*, XXXIX-B3:553–557.

Borchers, B., Marrero, S., Balco, G., Caffee, M., Goehring, B., Lifton, N., Nishiizumi, K., Phillips, F., Schaefer, J., and Stone, J. (2016). Geological calibration of spallation production rates in the CRONUS-Earth project. *Quaternary Geochronology*, 31:188–198. Publisher: Elsevier B.V ISBN: 4025594390.

Braucher, R., Guillou, V., Bourlès, D. L., Arnold, M., Aumaître, G., Keddadouche, K., and Nottoli, E. (2015). Preparation of ASTER in-house 10Be/9Be standard solutions. *Nuclear Instruments and Methods in Physics Research Section B: Beam Interactions with Materials and Atoms*, 361:335–340.

Braucher, R., Merchel, S., Borgomano, J., and Bourlès, D. (2011). Production of cosmogenic radionuclides at great depth: A multi element approach. *Earth and Planetary Science Letters*, 309(1-2):1–9.

Brown, E. T., Edmond, J. M., Raisbeck, G. M., Yiou, F., Kurz, M. D., and Brook, E. J. (1991). Examination of surface exposure ages of Antarctic moraines using in situ produced 10Be and 26Al. *Geochimica et Cosmochimica Acta*, 55(8):2269–2283. ISBN: 0016-7037.

Broxton, M. and Edwards, L. (2008). The Ames Stereo Pipeline: Automated 3D Surface Reconstruction from Orbital Imagery. In *Lunar and Planetary Science Conference*, volume 39, page 2419, League City, Texas. Series Title: Lunar and Planetary Science Conference.

Champagnac, J.-D., Molnar, P., Sue, C., and Herman, F. (2012). Tectonics, climate, and mountain topography. *Journal of Geophysical Research*, 117(B2):B02403.

Charreau, J., Blard, P.-H., Puchol, N., Avouac, J.-P., Lallier-Vergès, E., Bourlès, D., Braucher, R., Gallaud, A., Finkel, R., Jolivet, M., Chen, Y., and Roy, P. (2011). Paleo-erosion rates in Central Asia since 9Ma: A transient increase at the onset of Quaternary glaciations? *Earth and Planetary Science Letters*, 304(1-2):85–92.

Chueng, K. F., Gomes Coe, H. H., Ribeiro Rocha Augustin, C. H., Macario, K. D., Fricks Ricardo, S. D., and Carvalho Vasconcelos, A. M. (2019). Landscape paleodynamics in siliciclastic domains with the use of phytoliths, sponge spicules and carbon isotopes: The case of southern Espinhaço Mountain Range, Minas Gerais, Brazil. *Journal of South American Earth Sciences*, 95(April):102232. Publisher: Elsevier.

Cruz, F. W., Vuille, M., Burns, S. J., Wang, X., Cheng, H., Werner, M., Lawrence Edwards, R., Karmann, I., Auler, A. S., and Nguyen, H. (2009a). Orbitally driven east-west antiphasing of South American precipitation. *Nature Geoscience*, 2(3):210–214. Publisher: Nature Publishing Group.

Cruz, F. W., Wang, X., Auler, A., Vuille, M., Burns, S. J., Edwards, L. R., Karmann, I., and Cheng, H. (2009b). Orbital and Millennial-Scale Precipitation Changes in Brazil from Speleothem Records. In Vimeux, F., Sylvestre, F., and Khodri, M., editors, *Past Climate Variability in South America and Surrounding Regions*, volume 14, pages 29–60. Springer Netherlands, Dordrecht. Series Title: Developments in Paleoenvironmental Research.

DiBiase, R. A., Heimsath, A. M., and Whipple, K. X. (2012). Hillslope response to tectonic forcing in threshold landscapes. *Earth Surface Processes and Landforms*, 37(8):855–865.

DiBiase, R. A., Whipple, K. X., Heimsath, A. M., and Ouimet, W. B. (2010). Landscape form and millennial erosion rates in the San Gabriel Mountains, CA. *Earth and Planetary Science Letters*, 289(1-2):134–144.

Dietrich, W. E., Bellugi, D. G., Sklar, L. S., Stock, J. D., Heimsath, A. M., and Roering, J. J. (2003). Geomorphic transport laws for predicting landscape form and dynamics. In Wilcock, P. R. and Iverson, R. M., editors, *Prediction in Geomorphology*, volume

135, pages 103–132. American Geophysical Union, Washington, D. C. Series Title: Geophysical Monograph Series ISSN: 0065-8448.

Foster, M. A., Anderson, R. S., Wyshnytzky, C. E., Ouimet, W. B., and Dethier, D. P. (2015). Hillslope lowering rates and mobile-regolith residence times from in situ and meteoric 10Be analysis, Boulder Creek Critical Zone Observatory, Colorado. *Geological Society of America Bulletin*, 127(5):862–878.

Fox, M., Bodin, T., and Shuster, D. L. (2015). Abrupt changes in the rate of Andean Plateau uplift from reversible jump Markov Chain Monte Carlo inversion of river profiles. *Geomorphology*, 238:1–14. Publisher: Elsevier B.V.

Gabet, E. J., Burbank, D. W., Pratt-Sitaula, B., Putkonen, J., and Bookhagen, B. (2008). Modern erosion rates in the High Himalayas of Nepal. *Earth and Planetary Science Letters*, 267(3-4):482–494. ISBN: 0012-821X.

Gabet, E. J., Mudd, S. M., Wood, R. W., Grieve, S. W. D., Binnie, S. A., and Dunai, T. J. (2021). Hilltop Curvature Increases with the Square Root of Erosion Rate. *Journal of Geophysical Research: Earth Surface*, n/a(n/a):e2020JF005858. _eprint: https://onlinelibrary.wiley.com/doi/pdf/10.1029/2020JF005858.

Gaillardet, J., Dupré, B., Louvat, P., and Allègre, C. (1999). Global silicate weathering and CO2 consumption rates deduced from the chemistry of large rivers. *Chemical Geology*, 159(1-4):3–30.

Gelman, A. and Rubin, D. B. (1992). Inference from Iterative Simulation Using Multiple Sequences. *Statistical Science*, 7(4):457–472. arXiv: 1011.1669 ISBN: 0883-4237.

Godard, V., Dosseto, A., Fleury, J., Bellier, O., Siame, L., and ASTER, T. (2019). Transient landscape dynamics across the Southeastern Australian Escarpment. *Earth and Planetary Science Letters*, 506:397–406. Publisher: Elsevier B.V.

Godard, V., Hippolyte, J.-C., Cushing, E., Espurt, N., Fleury, J., Bellier, O., and Ollivier, V. (2020). Hillslope denudation and morphologic response to a rock uplift gradient. *Earth Surface Dynamics*, 8(2):221–243.

Godard, V., Ollivier, V., Bellier, O., Miramont, C., Shabanian, E., Fleury, J., Benedetti, L., and Guillou, V. (2016). Weathering-limited hillslope evolution in carbonate landscapes. *Earth and Planetary Science Letters*, 446:10–20. Publisher: Elsevier B.V.

Granger, D. E., Kirchner, J. W., and Finkel, R. (1996). Spatially averaged long-term erosion rates measured from in situ-produced cosmogenic nuclides in alluvial sediment. *The Journal of Geology*, 104(3):249–257.

Granger, D. E. and Muzikar, P. F. (2001). Dating sediment burial with in situ-produced cosmogenic nuclides: theory, techniques, and limitations. *Earth and Planetary Science Letters*, 188(1-2):269–281. ISBN: 0012-821X.

Grieve, S. W., Mudd, S. M., and Hurst, M. D. (2016a). How long is a hillslope? *Earth Surface Processes and Landforms*, 41(8):1039–1054.

Grieve, S. W. D., Mudd, S. M., Hurst, M. D., and Milodowski, D. T. (2016b). A nondimensional framework for exploring the relief structure of landscapes. *Earth Surface Dynamics*, 4(2):309–325.

Hales, T. C. and Roering, J. J. (2005). Climate-controlled variations in scree production, Southern Alps, New Zealand. *Geology*, 33(9):701–704.

Herman, F. and Champagnac, J.-D. (2016). Plio-Pleistocene increase of erosion rates in mountain belts in response to climate change. *Terra Nova*, 28(1):2–10.

Hippe, K. (2017). Constraining processes of landscape change with combined in situ cosmogenic 14 C- 10 Be analysis. *Quaternary Science Reviews*, 173:1–19. Publisher: Elsevier Ltd.

Hippe, K., Jansen, J. D., Skov, D. S., Lupker, M., Ivy-Ochs, S., Kober, F., Zeilinger, G., Capriles, J. M., Christl, M., Maden, C., Vockenhuber, C., and Egholm, D. L. (2021). Cosmogenic in situ 14 C- 10 Be reveals abrupt Late Holocene soil loss in the Andean Altiplano. *Nature Communications*, 12(1):2546. Number: 1 Publisher: Nature Publishing Group.

Hurst, M. D., Mudd, S. M., Attal, M., and Hilley, G. (2013). Hillslopes record the growth and decay of landscapes. *Science*, 341(6148):868–871.

Hurst, M. D., Mudd, S. M., Walcott, R., Attal, M., and Yoo, K. (2012). Using hilltop curvature to derive the spatial distribution of erosion rates. *Journal of Geophysical Research*, 117(F2):F02017.

Knudsen, M. F. and Egholm, D. L. (2018). Constraining Quaternary ice covers and erosion rates using cosmogenic 26Al/10Be nuclide concentrations. *Quaternary Science Reviews*, 181:65–75. Publisher: Elsevier Ltd.

Knudsen, M. F., Egholm, D. L., and Jansen, J. D. (2019). Time-integrating cosmogenic nuclide inventories under the influence of variable erosion, exposure, and sediment mixing. *Quaternary Geochronology*, 51(December 2018):110–119. Publisher: Elsevier.

Laloy, E., Beerten, K., Vanacker, V., Christl, M., Rogiers, B., and Wouters, L. (2017). Bayesian inversion of a CRN depth profile to infer Quaternary erosion of the northwestern Campine Plateau (NE Belgium). *Earth Surface Dynamics*, 5(3):331–345.

Lashermes, B., Foufoula-Georgiou, E., and Dietrich, W. E. (2007). Channel network extraction from high resolution topography using wavelets. *Geophysical Research Letters*, 34(23):L23S04. ISBN: 0094-8276.

Ledru, M. P., Rousseau, D. D., Cruz, F. W., Riccomini, C., Karmann, I., and Martin, L. (2005). Paleoclimate changes during the last 100,000 yr from a record in the Brazilian Atlantic rainforest region and interhemispheric comparison. *Quaternary Research*, 64(3):444–450.

Lenard, S. J., Lavé, J., France-Lanord, C., Aumaître, G., Bourlès, D. L., and Keddadouche, K. (2020). Steady erosion rates in the Himalayas through late Cenozoic climatic changes. *Nature Geoscience*, 13(6):448–452. Publisher: Springer US.

Lifton, N., Sato, T., and Dunai, T. J. (2014). Scaling in situ cosmogenic nuclide production rates using analytical approximations to atmospheric cosmic-ray fluxes. *Earth and Planetary Science Letters*, 386:149–160. Publisher: Elsevier B.V.

Lisiecki, L. E. and Raymo, M. E. (2005). A Pliocene-Pleistocene stack of 57 globally distributed benthic d18O records. *Paleoceanography*, 20(1):PA1003. Publisher: American Geophysical Union.

Magalhães Junior, A. P., de Paula Barros, L. F., and Felippe, M. F. (2015). Southern Serra do Espinhaço: The Impressive Plateau of Quartzite Ridges. In Vieira, B. C., Salgado, A. A. R., and Santos, L. J. C., editors, *Landscapes and landforms of Brazil*, pages 359–370. Springer. ISSN: 22132104.

Makhubela, T., Kramers, J., Scherler, D., Wittmann, H., Dirks, P., and Winkler, S. (2019). Effects of long soil surface residence times on apparent cosmogenic nuclide denudation rates and burial ages in the Cradle of Humankind, South Africa. *Earth Surface Processes and Landforms*, 44(15):2968–2981.

Merchel, S., Arnold, M., Aumaître, G., Benedetti, L., Bourlès, D., Braucher, R., Alfimov, V., Freeman, S., Steier, P., and Wallner, A. (2008). Towards more precise 10Be and 36Cl data from measurements at the 10-14 level: Influence of sample preparation. *Nuclear Instruments and Methods in Physics Research Section B: Beam Interactions with Materials and Atoms*, 266(22):4921–4926.

Merchel, S. and Bremser, W. (2004). First international 26Al interlaboratory comparison - Part I. *Nuclear Instruments and Methods in Physics Research Section B: Beam Interactions with Materials and Atoms*, 223-224:393–400. Publisher: North-Holland.

Metropolis, N., Rosenbluth, A. W., Rosenbluth, M. N., Teller, A. H., and Teller, E. (1953). Equation of State Calculations by Fast Computing Machines. *The Journal of Chemical Physics*, 21(6):1087–1092.

Moratto, Z., Broxton, M., Beyer, R., Lundy, M., and Husmann, K. (2010). Ames Stereo Pipeline, NASA's Open Source Automated Stereogrammetry Software. In *Lunar and Planetary Science Conference*, volume 41, page 2364, The Woodlands, Texas. Series Title: Lunar and Planetary Science Conference.

720 Mudd, S. M. (2016). Detection of transience in eroding landscapes. *Earth Surface Processes*
721 *and Landforms*, 42(1):24–41. ISBN: 0197-9337.

722 Nefian, A. V., Husmann, K., Broxton, M., To, V., Lundy, M., and Hancher, M. D. (2009).
723 A bayesian formulation for sub-pixel refinement in stereo orbital imagery. In *2009 16th*
724 *IEEE International Conference on Image Processing (ICIP)*, pages 2361–2364, Cairo,
725 Egypt. IEEE.

726 Norton, K. P. and Schlunegger, F. (2017). Lack of a weathering signal with increased
727 Cenozoic erosion? *Terra Nova*, 29(5):265–272.

728 Ouimet, W. B., Whipple, K. X., and Granger, D. E. (2009). Beyond threshold hillslopes:
729 Channel adjustment to base-level fall in tectonically active mountain ranges. *Geology*,
730 37(7):579–582. Publisher: Geological Society of America.

731 Peifer, D., Persano, C., Hurst, M. D., Bishop, P., and Fabel, D. (2020). Growing topography
732 due to contrasting rock types in a tectonically dead landscape. *Earth Surface Dynamics*
733 *Discussions*, 2020:1–29.

734 Roberts, G. G. and White, N. (2010). Estimating uplift rate histories from river profiles
735 using African examples. *Journal of Geophysical Research*, 115(B2):B02406.

736 Roering, J. J., Almond, P., Tonkin, P., and McKean, J. (2004). Constraining climatic
737 controls on hillslope dynamics using a coupled model for the transport of soil and trac-
738 ers: Application to loess-mantled hillslopes, South Island, New Zealand. *Journal of*
739 *Geophysical Research*, 109(F1):F01010. ISBN: 0148-0227.

740 Roering, J. J., Kirchner, J. W., and Dietrich, W. E. (1999). Evidence for nonlinear,
741 diffusive sediment transport on hillslopes and implications for landscape morphology.
742 *Water Resources Research*, 35(3):853–870. Publisher: American Geophysical Union.

743 Roering, J. J., Kirchner, J. W., and Dietrich, W. E. (2001). Hillslope evolution by nonlin-
744 ear, slope-dependent transport: Steady state morphology and equilibrium adjustment
745 timescales. *Journal of Geophysical Research*, 106(B8):16499–16513. ISBN: 0148-0227.

746 Roering, J. J., Marshall, J., Booth, A. M., Mort, M., and Jin, Q. (2010). Evidence for
747 biotic controls on topography and soil production. *Earth and Planetary Science Letters*,
748 298(1-2):183–190. Publisher: Elsevier B.V. ISBN: 0012-821X.

749 Roering, J. J., Perron, J. T., and Kirchner, J. W. (2007). Functional relationships between
750 denudation and hillslope form and relief. *Earth and Planetary Science Letters*, 264(1-
751 2):245–258.

752 Salgado, A. A. R., Rezende, E. d. A., Bourlès, D., Braucher, R., da Silva, J. R., and Garcia,
753 R. A. (2016). Relief evolution of the Continental Rift of Southeast Brazil revealed by in
754 situ-produced 10Be concentrations in river-borne sediments. *Journal of South American*
755 *Earth Sciences*, 67:89–99.

Salgado, A. A. R., Santos, L. J. C., and Paisani, J. C. (2019). *The physical geography of Brazil*. Springer. Publication Title: Springer.

Salgado-Labouriau, M. L., Barberi, M., Ferraz-Vicentini, K. R., and Parizzi, M. G. (1998). A dry climatic event during the late Quaternary of tropical Brazil. *Review of Palaeobotany and Palynology*, 99(2):115–129.

Silva, A. C., Horàk-Terra, I., Barral, U. M., Costa, C. R., Gonçalves, S. T., Pinto, T., Christófaro Silva, B. P., Cunha Fernandes, J. S., Mendonça Filho, C. V., and Vidal-Torrado, P. (2020). Altitude, vegetation, paleoclimate, and radiocarbon age of the basal layer of peatlands of the Serra do Espinhaço Meridional, Brazil. *Journal of South American Earth Sciences*, 103(June):102728.

Skov, D. S., Egholm, D. L., Jansen, J. D., Sandiford, M., and Knudsen, M. F. (2019). Detecting landscape transience with in situ cosmogenic 14C and 10Be. *Quaternary Geochronology*, 54(June):101008.

Stone, J. O. (2000). Air pressure and cosmogenic isotope production. *Journal of Geophysical Research: Solid Earth*, 105(B10):23753–23759. Publisher: American Geophysical Union.

Struck, M., Jansen, J. D., Fujioka, T., Codilean, A. T., Fink, D., Egholm, D. L., Fülöp, R.-H., Wilcken, K. M., and Kotevski, S. (2018). Soil production and transport on postorogenic desert hillslopes quantified with 10Be and 26Al. *GSA Bulletin*, 130(5-6):1017–1040.

von Blanckenburg, F. (2005). The control mechanisms of erosion and weathering at basin scale from cosmogenic nuclides in river sediment. *Earth and Planetary Science Letters*, 237(3-4):462–479.

Wang, X., Auler, A. S., Edwards, R. L., Cheng, H., Ito, E., Wang, Y., Kong, X., and Solheid, M. (2007). Millennial-scale precipitation changes in southern Brazil over the past 90,000 years. *Geophysical Research Letters*, 34(23):L23701. Publisher: American Geophysical Union.

West, N., Kirby, E., Bierman, P., and Clarke, B. A. (2014). Aspect-dependent variations in regolith creep revealed by meteoric 10Be. *Geology*, 42(6):507–510.

Willenbring, J. K. and Jerolmack, D. J. (2016). The null hypothesis: globally steady rates of erosion, weathering fluxes and shelf sediment accumulation during Late Cenozoic mountain uplift and glaciation. *Terra Nova*, 28(1):11–18.

Table 1: Cosmogenic nuclides data : ^{10}Be results

	Mass[a] (g)	Be carrier[b] (g)	^{10}Be/^{9}Be[c,d,e,f] ($\times 10^{-12}$)	[^{10}Be][d] ($\times 10^{6}$ at/g)	^{10}Be denudation rate[d,g,h] (m/Ma)	τ[i] (Ma)
M	16.22	0.1521	0.624 ± 0.013	1.176 ± 0.024	3.69 ± 0.33 (3.46)	0.2
N	16.84	0.1531	1.23 ± 0.02	2.254 ± 0.037	1.84 ± 0.17 (1.67)	0.3
O	9.8	0.153	0.573 ± 0.014	1.798 ± 0.045	2.37 ± 0.24 (2.19)	0.3
P	20.87	0.1529	2.999 ± 0.048	4.437 ± 0.071	0.83 ± 0.09 (0.68)	0.7
Q	21.85	0.1519	4.898 ± 0.073	6.879 ± 0.103	0.5 ± 0.06 (0.33)	1.2
R	21.65	0.1527	5.048 ± 0.072	7.192 ± 0.103	0.46 ± 0.06 (0.29)	1.3
S	21.17	0.1543	3.966 ± 0.06	5.838 ± 0.089	0.61 ± 0.07 (0.45)	1.0
T	17.82	0.1533	5.205 ± 0.076	9.046 ± 0.132	0.35 ± 0.05 (0.18)	1.7
U	20.11	0.1475	0.516 ± 0.011	0.759 ± 0.017	6 ± 0.54 (5.7)	0.1
V	19.77	0.1525	1.139 ± 0.02	1.77 ± 0.031	2.32 ± 0.21 (2.14)	0.3
W	20.02	0.1536	2.902 ± 0.053	4.495 ± 0.082	0.82 ± 0.09 (0.67)	0.7

[a] Dissolved pure quartz mass.

[b] Be in-house carrier mass, ∼150 μl at 3.025 x 10^{-3} g/g [Merchel et al., 2008].

[c] ^{10}Be/^{9}Be ratios were calibrated against the STD-11 standard by using an assigned value of $1.191 \pm 0.013 \times 10^{-11}$ [Braucher et al., 2015].

[d] Uncertainties are reported at the 1σ level.

[e] Uncertainties on isotopic ratios are calculated according to the standard error propagation method using the quadratic sum of the relative errors and include a conservative 0.5% external machine uncertainty [Arnold et al., 2010], the uncertainty on the certified standard ratio, a 1σ uncertainty associated to the mean of the standard ratio measurements during the measurement cycles, a 1σ statistical error on counted events and the uncertainty associated with the chemical and analytical blank corrections.

[f] One process blank was treated and measured with our samples, yielding a ^{10}Be/^{9}Be ratio of $3.53 \pm 0.34 \times 10^{-15}$. It corresponds to an upper 1σ bound of 120 $\times 10^{3}$ ^{10}Be atoms for the background level in this blank, which is at least 120 times lower than the number of ^{10}Be atoms in the dissolved sample masses (600 times lower in average over our dataset).

[g] Denudation rates were calculated with the online calculator described in Balco et al. [2008] and the nuclide specific LSD scaling scheme [Lifton et al., 2014], using the CRONUS-Earth calibration dataset [Borchers et al., 2016] for the calculation of spallation production rates and muon production rates according to Balco [2017]. We use 160 g/cm^2 for the effective neutron attenuation length in rock, and a density of 2.65 g/cm^3. No shielding correction was considered for the hilltop sites we sampled.

[h] Numbers in parenthesis are the denudation rates computed with Lal/Stone time-independent scaling.

[i] Integration time scales for ^{10}Be denudation rates [von Blanckenburg, 2005].

Table 2: Cosmogenic nuclides data : ^{26}Al results and comparison with ^{10}Be results from table 1

Sample	[Al] natural[a] (ppm)	Al carrier[b] (g)	^{26}Al/^{27}Al[c,d,e] ($\times 10^{-12}$)	[^{26}Al][d] ($\times 10^{6}$ at/g)	^{26}Al denudation rate[f] (mm/ka)	τ[g] (Ma)	^{10}Be/^{26}Al
M	17.8	1.2448	3.749 ± 0.12	7.27 ± 0.236	3.76 ± 0.54	0.2	6.18 ± 0.24
N	16.1	1.2227	7.834 ± 0.199	14.327 ± 0.369	1.67 ± 0.26	0.4	6.36 ± 0.19
O	114.3	0.6983	3.534 ± 0.105	11.589 ± 0.352	2.2 ± 0.34	0.3	6.44 ± 0.25
P	17.3	1.2211	16.83 ± 0.282	24.976 ± 0.43	0.79 ± 0.15	0.8	5.63 ± 0.13
Q	23.2	1.2278	20.568 ± 0.316	30.037 ± 0.475	0.62 ± 0.13	1.0	4.37 ± 0.1
R	60.4	1.0101	31.101 ± 0.484	45.586 ± 0.727	0.32 ± 0.1	1.9	6.34 ± 0.14
S	20.9	1.2229	21.864 ± 0.346	32.577 ± 0.53	0.56 ± 0.12	1.1	5.58 ± 0.12
T	20.7	1.2355	24.249 ± 0.391	43.197 ± 0.716	0.37 ± 0.1	1.6	4.78 ± 0.11
U	17.9	1.1851	3.256 ± 0.098	4.867 ± 0.149	6.05 ± 0.81	0.1	6.41 ± 0.24
V	16.9	1.0800	7.835 ± 0.208	10.91 ± 0.294	2.27 ± 0.34	0.3	6.16 ± 0.2
W	22.0	1.1442	17.57 ± 0.303	26.155 ± 0.462	0.74 ± 0.14	0.8	5.82 ± 0.15

[a] Naturally occurring Al measured by ICP-OES. Note the high concentration for sample O, which is the only one from the quartzite bedrock instead of the quartz veins.

[b] Al Carrier mass, 993±4 ppm concentration.

[c] The measured ^{26}Al/^{27}Al ratios were normalized to the in-house standard SM-Al-11 whose ratio of $7.401 \pm 0.064 \times 10^{-12}$ [Arnold et al., 2010] has been cross-calibrated against primary standards from a round-robin exercise [Merchel and Bremser, 2004].

[d] Uncertainties are reported at the 1σ level.

[e] A process blank yielded a ratio of $2.01 \pm 0.45 \times 10^{-14}$. It corresponds to an upper 1σ bound of 730 $\times 10^3$ ^{26}Al atoms for the background level in this blank, which is at least 130 times lower than the number of ^{26}Al atoms in the dissolved sample masses (610 times lower in average over our dataset)

[f] Procedures for the calculation of denudation rates are identical to the ones described in table 1.

[g] Integration time scales for ^{26}Al denudation rates [von Blanckenburg, 2005].

Table 3: Site locations and hilltop curvature measurements

Site	Latitude (^{o})	Longitude (^{o})	Altitude (m)	Hilltop curvature (m^{-1})
M	-19.2637	-43.5558	1313	0.028±0.010
N	-19.2614	-43.5508	1354	0.020±0.008
O	-19.2612	-43.5508	1353	0.039±0.010
P	-19.2361	-43.5058	1355	0.006±0.002
Q	-19.2301	-43.5051	1365	0.005±0.001
R	-19.2119	-43.5027	1335	0.008±0.001
S	-19.1594	-43.5156	1380	0.008±0.003
T	-19.1582	-43.5174	1379	0.007±0.003
U	-19.2206	-43.4989	1337	0.038±0.011
V	-19.2218	-43.4968	1301	0.024±0.007
W	-19.2337	-43.5050	1357	0.014±0.003